Supporting Information

Combining NMR and Impedance Spectroscopy In-Situ to Study the Dynamics of Solid Ion Conductors

Sheyi Clement Adediwura[1], Neeshma Mathew[1], Jörn Schmedt auf der Günne[*1]

[1]University of Siegen, Faculty IV: School of Science and Technology, Department of Chemistry and Biology, Inorganic Materials Chemistry, Adolf-Reichwein-Straße 2, 57068 Siegen, Germany
*Corresponding author: gunnej@chemie.uni-siegen.de

Table of Contents

S1 3D Printing

Table S1: 3D printers and printing conditions with corresponding filaments such as; acrylonitrile butadiene styrene (ABS), polyether ether ketone (PEEK) and polyphenylene sulfone (PPSU).

Printer	Creality CR-10s	Intamsys Funmat HT	
Material	ABS	PEEK	PPSU
Manufacturer	BASF	3D4Makers	BASF
Bed surface	3DLAC spray	Elmer's Glue Stick	Elmer's Glue Stick
Nozzle diameter/mm	0.4	0.25	0.25
T_{nozzle}/K	528	673	683
T_{bed}/K	383	418	418

S2 Decoupling of NMR and EIS Channels

Low and high pass filter circuits were simulated using VIPEC software v3.2.1[3] and the fabricated circuits' performance was checked with scattering parameter measurements using a vector network analyser. Figure S1 shows the response of the fabricated filter.

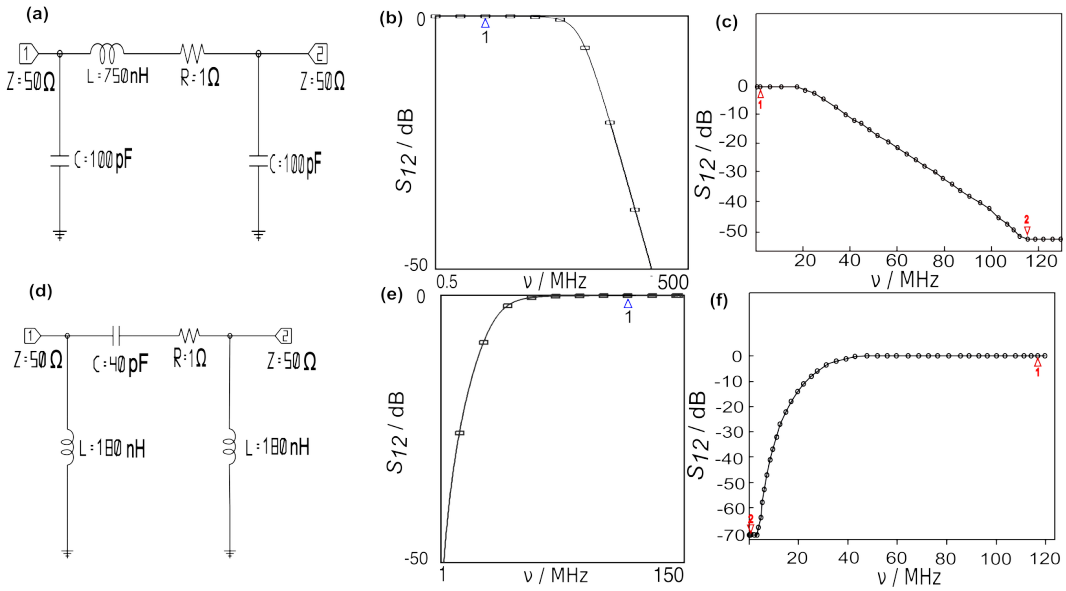

Figure S1: (a) Passive low pass filter circuit. (b) Simulated response of the low pass filter using Vipec software v3.1.2-1.[3] (c) Bode plot of the fabricated low pass filter with 56.1 dB attenuation at 116.6 MHz ^{7}Li NMR (7 T) Larmor frequency measured using vector network analyser. (d) Passive high pass filter circuit. (e) Simulated response of the high pass filter using Vipec software v3.2.1.[3] (f) Bode plot of the fabricated high pass filter with 71.5 dB attenuation at 2 MHz measured using vector network analyser.

S3 Calibration and Validation of the EIS Channel

The EIS channel of the in-situ NMR-EIS setup consist of a long BNC cable (5 m) and four units of low pass filters connected to the EIS channel. Therefore, the sample's impedance needs to be isolated from that of the four low-pass filters' components and the inductance of the BNC cable. Short, and load (100 Ω) calibrations were performed to isolate the residual fixtures, using fabricated standards adapted to the sample's configuration for effective calibrations.

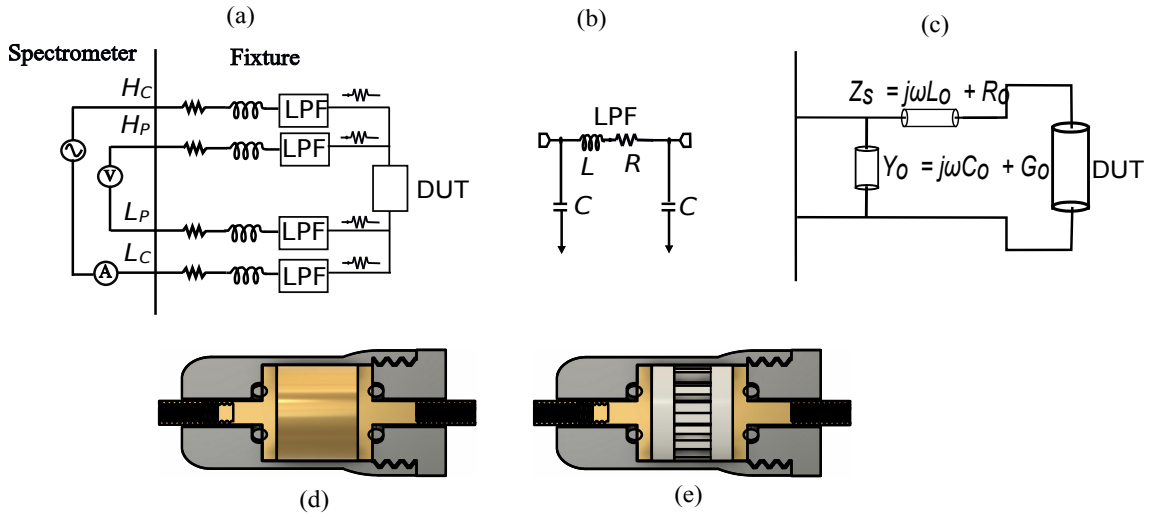

Figure S2: (a) In-situ EIS channel circuit diagram in 4-wire terminal pair configuration with low pass filter circuit. (b) Low pass filter circuit diagram. (c) Residual impedance and stray admittance error circuit diagram. Fabricated calibration sets adapted to the size and position of the sample, (d) short circuit impedance calibration with a brass disc making a contact between the electrodes. (e) Load impedance calibration using 100 Ω resistor.

Upon completion of all calibration steps, a known impedance load (R = 100 Ω) was measured. Figure S3 shows the calibration was successful.

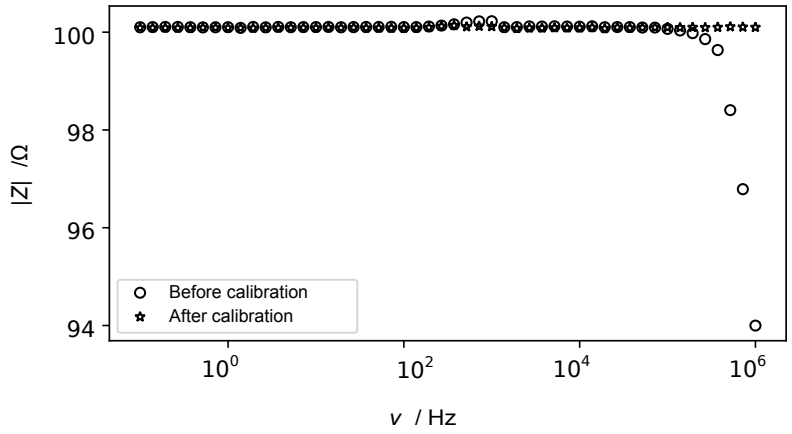

Figure S3: Impedance measurement of 100 Ω resistor before and after short/load calibration.

Furthermore, the impedance of 3 mm thick and 8 mm diameter $Li_{1.5}Al_{0.5}Ge_{1.5}(PO_4)_3$ pellet was recorded five times each. For both ex-situ EIS and in-situ NMR-EIS configurations. The ex-situ EIS consists of a standard EIS measurement setup with 0.5 m long BNC cable, connected to a home-built airtight two-electrode cell, while the in-situ NMR-EIS setup consists of four low pass filters with 5 m long BNC cables connected to the developed in-situ NMR-EIS cell. The impedance data of $Li_{1.5}Al_{0.5}Ge_{1.5}(PO_4)_3$ via in-situ NMR-EIS channel are in excellent agreement with the standard impedance data and reproducible (Figure S4). The data analysis results show that both ex-situ EIS and in-situ NMR-EIS channel measurements are in excellent agreement and reproducible.

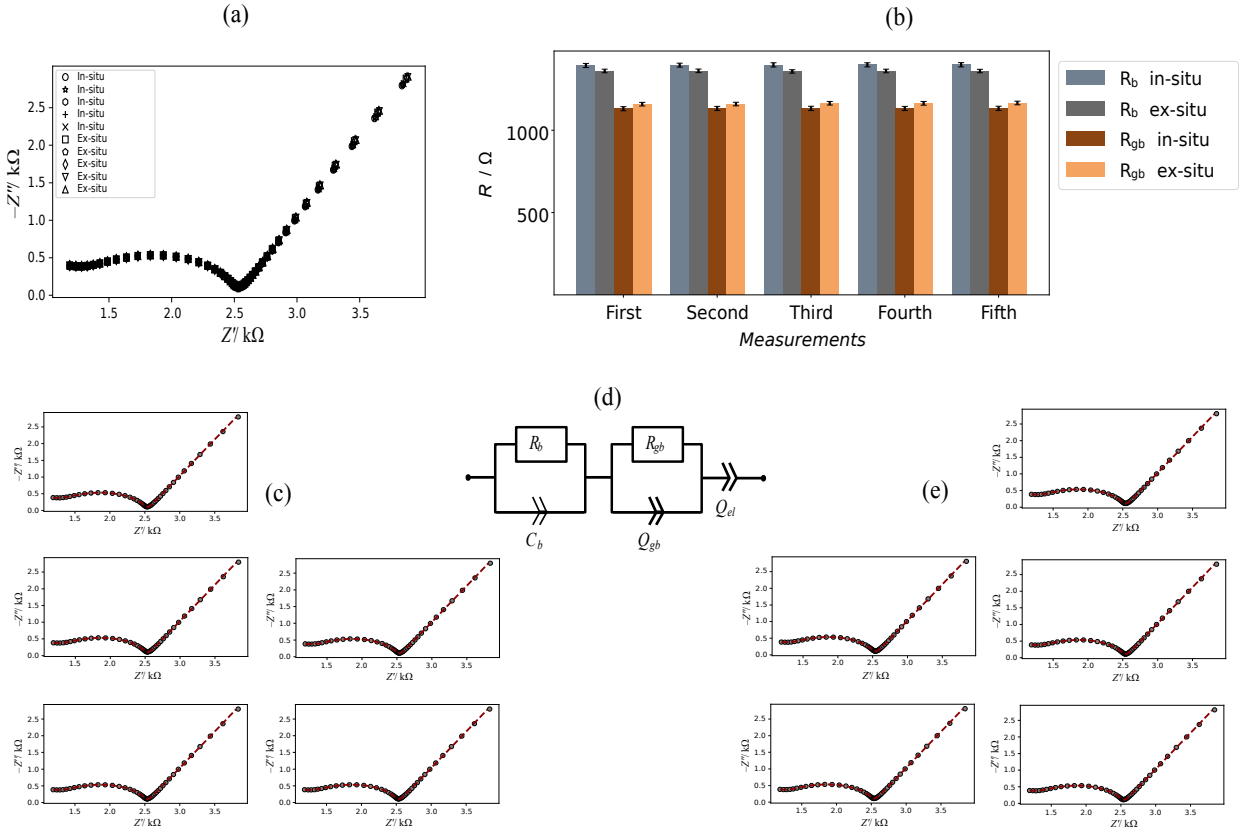

Figure S4: Validation result of $Li_{1.5}Al_{0.5}Ge_{1.5}(PO_4)_3$ showing; (a) Stacked Nyquist plots of five rounds of impedance measurement via in-situ NMR-EIS channel with 5 m BNC cable connected to four low pass filters in a 4-wire measurement configuration and ex-situ EIS standard setup with 0.5 m BNC cable, recorded using 10 mV A.C. voltage at 20.3 °C. (b) Respective resistance value obtained from the fitting of the in-situ data set (c) and ex-situ data set (e), using an equivalent circuit based on brick layer model.[5] (d) Bricklayer model for impedance data analysis Here, R_b and R_{gb} are the bulk and grain boundary resistance, C_b, is the bulk capacitance, while Q_{gb} and Q_{el} represent the constant phase element for the grain boundary and the electrode polarisation region, respectively.

Table S2: Validation of the calibration procedure showing detailed impedance data analysis of $Li_{1.5}Al_{0.5}Ge_{1.5}(PO_4)_3$ recorded five times each, for both standard ex-situ EIS and in-situ NMR-EIS configurations after calibration. The analysis were performed using home-written python scripts based on the SciPy libraries.[4] The fit model is shown in Figure S4d, the five data sets were fitted together using a single χ^2 value (i.e., χ^2=0.007 and χ^2=0.006 for ex-situ and in-situ data, respectively), which reduces the number of overall fitted parameters. The values of the fitted parameters are given below, where R_b and R_{gb} are bulk and grain boundary resistance, C_b bulk capacitance, Q_{gb} and Q_{el} representing the constant phase element for the grain boundary and the electrode polarisation region, respectively. The parameter α is the Q exponent describing the phase shift. The data fitting was performed such that only a single C_b was used to fit the five data sets for both in-situ and ex-situ. The correlation matrix was analysed and linear dependencies with a correlation factor |C| > 0.87 were not found for the resistance values.

Impedance measurements		R_b / Ω	R_{gb} / Ω	C_b / F	Q_{gb} / F	α_{gb}	Q_{el} / F	α_{el}
Ex-situ	i.	1194.3(4)	1331.2(6)	$2.70\ (2)\cdot10^{-11}$	$1.26\ (6)\cdot10^{-08}$	0.830(4)	$1.54\ (1)\cdot10^{-05}$	0.730(2)
	ii.	1194.7(4)	1332.6(6)		$1.26\ (6)\cdot10^{-08}$	0.830(4)	$1.53\ (1)\cdot10^{-05}$	0.730(2)
	iii.	1195.0(4)	1333.6(6)		$1.26\ (6)\cdot10^{-08}$	0.830(4)	$1.53\ (1)\cdot10^{-05}$	0.730(2)
	iv.	1195.7(4)	1335.0(6)		$1.26\ (6)\cdot10^{-08}$	0.830(4)	$1.53\ (1)\cdot10^{-05}$	0.730(2)
	v.	1195.6(4)	1336.8(6)		$1.27\ (6)\cdot10^{-08}$	0.830(4)	$1.52\ (1)\cdot10^{-05}$	0.730(2)
In-situ	i.	1191.9(5)	1340.0(6)	$2.85\ (2)\cdot10^{-11}$	$1.29\ (6)\cdot10^{-08}$	0.828(4)	$1.59\ (1)\cdot10^{-05}$	0.729(2)
	ii.	1193.6(5)	1341.9(6)		$1.29\ (6)\cdot10^{-08}$	0.828(4)	$1.58\ (1)\cdot10^{-05}$	0.729(2)
	iii.	1194.3(5)	1343.0(6)		$1.29\ (6)\cdot10^{-08}$	0.828(4)	$1.58\ (1)\cdot10^{-05}$	0.729(2)
	iv.	1194.4(5)	1343.3(6)		$1.29\ (6)\cdot10^{-08}$	0.828(4)	$1.58\ (1)\cdot10^{-05}$	0.729(2)
	v.	1194.2(5)	1344.0(6)		$1.29\ (6)\cdot10^{-08}$	0.828(4)	$1.57\ (1)\cdot10^{-05}$	0.729(2)

S4 Design and Fabrication of an In-situ NMR-EIS Probe Head

Here, all channels were integrated, and the in-situ NMR-EIS probe head was developed.

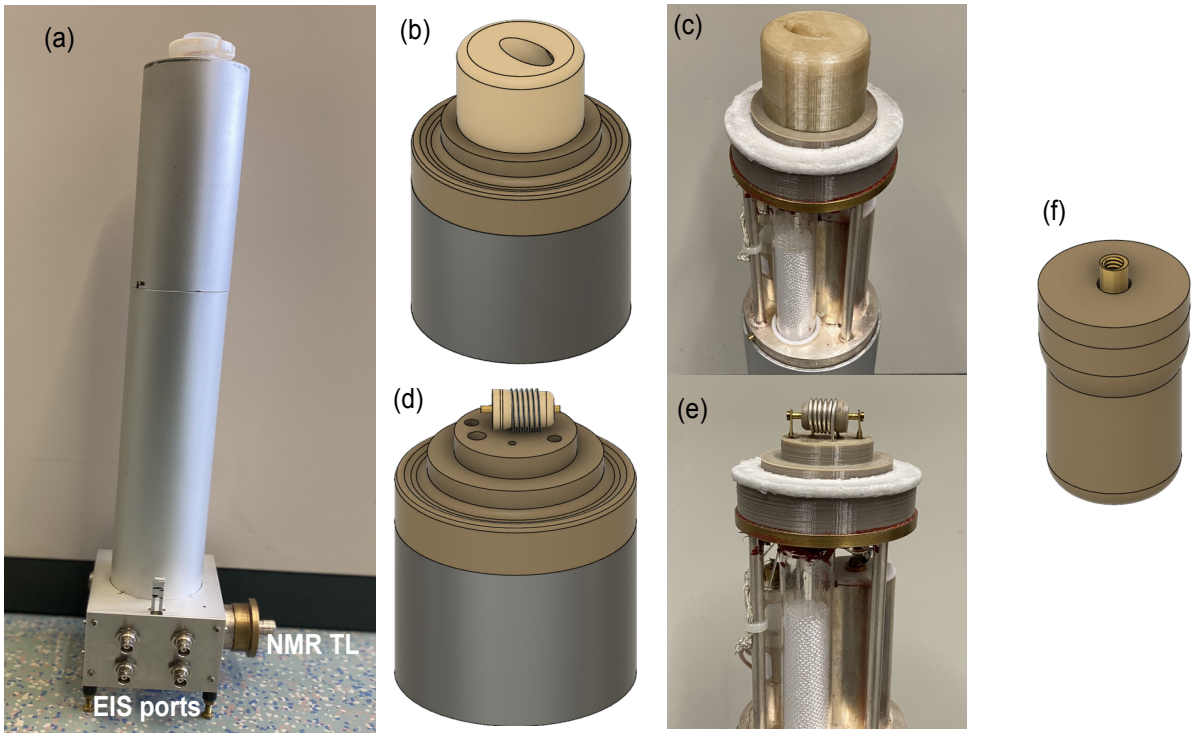

Figure S5: In-situ NMR-EIS probe-head. (a) Image showing the full in-situ NMR-impedance spectroscopy setup. (b) 3D model showing the top part of the in-situ probe-head for variable temperature experiment. (c) 3D printed top part of the in-situ probe-head suitable for variable temperature (173 K to 473 K). (d) 3D model showing the top part of the probe-head with mounted sample cell. (e) 3D printed top part of the in-situ probe-head with mounted sample cell inside the NMR coil and connected to the impedance spectrometer. (f) 3D model of in-situ sample cell.

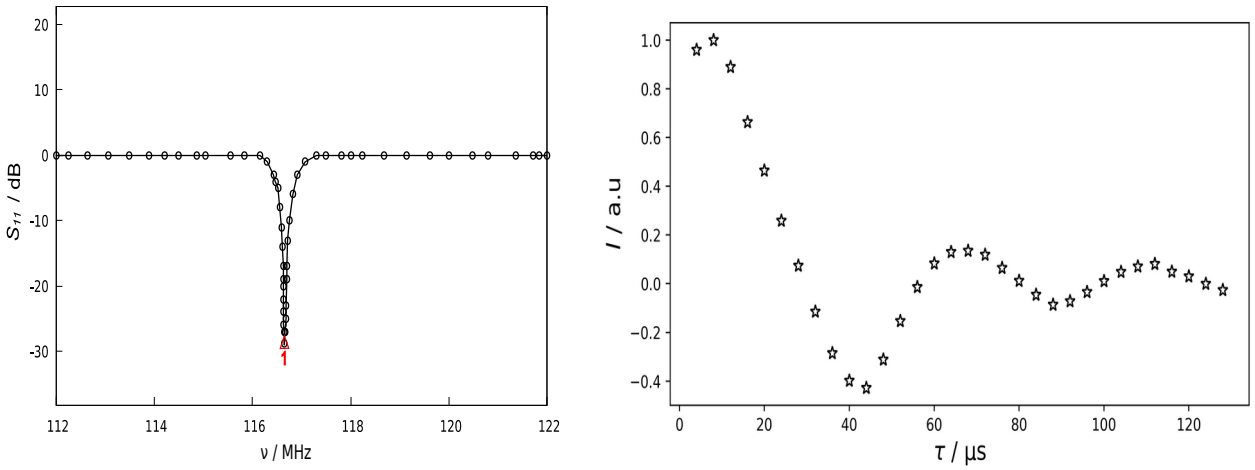

Figure S6: (a) Scattering parameter of the in-situ NMR-EIS probe-head tuned to ^{7}Li NMR resonance frequency (116.643 MHz), measured using a vector network analyser. (b)^{7}Li NMR nutation curve of LiCl.

S5 Solid State Synthesis of $Li_{1.5}Al_{0.5}Ge_{1.5}(PO_4)_3$

The stoichiometric ratio of Li_2CO_3 (0.796 g, 0.011 mol), Al_2O_3 (0.366 g, 0.004 mol), GeO_2 (2.254 g, 0.022 mol), $(NH_4)_2HPO_4$ (5.517 g, 0.043 mol) were measured and ground using a ball mill at 30 Hz for 30 min. It was then heated at 673 K for 2 hours at a heating rate of 2 K/min to decompose $(NH_4)_2HPO_4$ and Li_2CO_3. The resulting sample was re-ground into a fine powder using ball mill for 8 hours at 30 Hz, then heated in a platinum crucible at 1173 K with 3 K/min ramp rate for 3 hours. The obtained result was ground using ball mill for 8 hours at 30 Hz to obtain a final powder.

S6 Phase Characterization

S6.1 Li_8SnO_6

Figure S7 shows Rietveld refinement analysis of Li_8SnO_6 with fitting parameters R_p, R_{exp} and *gof* of 4.4 %, 5.0 % and 1.3 %, respectively. The refinement reveals that the sample contains Li_2O as a side phase of about 0.81 % due to the excess of Li_2O added during the preparation to compensate for the Li loss during high temperature solid state synthesis. The sample exhibits trigonal ($R\bar{3}$, a = 5.4690(1) Å, c = 15.2987(4) Å) symmetry with lithium atoms occupying the tetrahedral and octahedral sites of the slightly distorted hexagonal closed packed of oxygen atoms.[1] The compound Li_8SnO_6 has two different Wyckoff positions *18f* and *6c* for Li atoms. The ^{117}Sn NMR exhibits a single sharp peak at δ_{iso} = 496 ppm which is due to the SnO_6 units in the crystal structure.

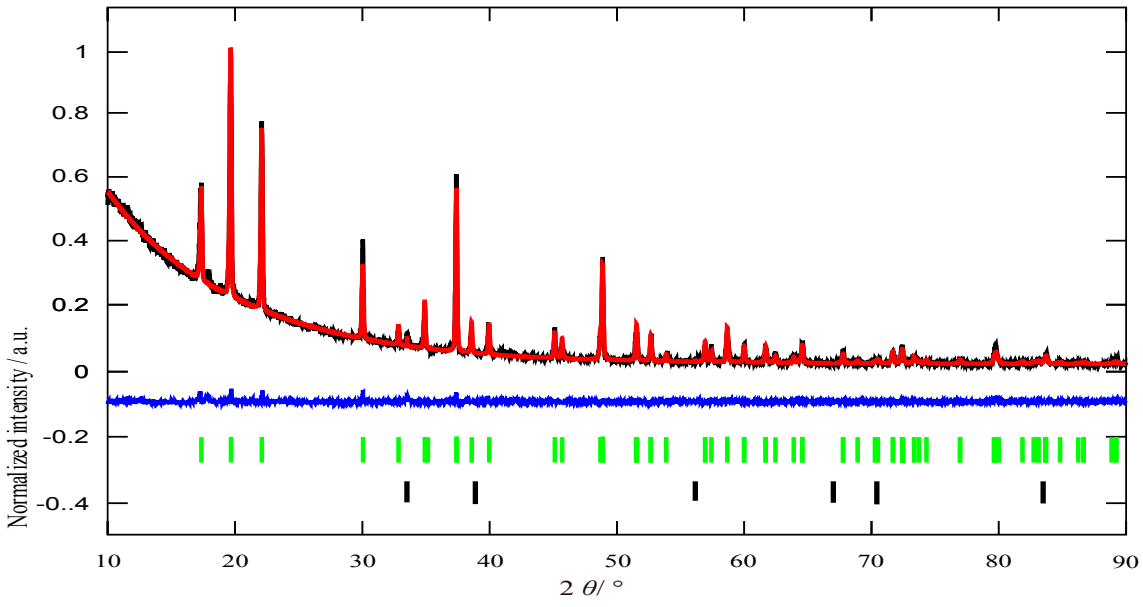

Figure S7: Observed (black line) powder diffraction pattern of Li_8SnO_6 measured with Cu $K\alpha_1$ radiation (λ=1.54056 Å) and calculated diffraction pattern (red lines) using the Rietveld refinement. The blue line represents the difference profile, while the vertical green and black lines are peak positions of Li_8SnO_6 (ICSD-28016) and Li_2O, respectively.

S6.2 $Li_{1.5}Al_{0.5}Ge_{1.5}(PO_4)_3$

The recorded X-ray diffractograms of $Li_{1.5}Al_{0.5}Ge_{1.5}(PO_4)_3$ powder pattern is shown below. It was plotted with the obtained literature diffractograms of $LiGe_2(PO_4)_3$.[2]

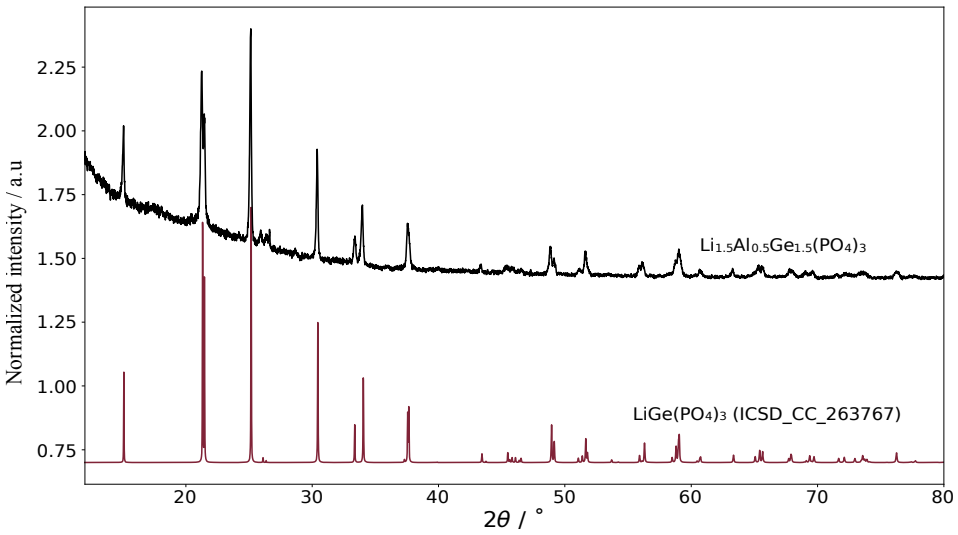

Figure S8: Powder diffraction pattern of $Li_{1.5}Al_{0.5}Ge_{1.5}(PO_4)_3$ measured with Cu $K\alpha_1$ radiation (λ=1.54056 Å) as compared to powder diffraction pattern of $LiGe_2(PO_4)_3$ obtained from literature.[2]

S7 Ex-situ and In-situ Impedance Spectroscopy Analysis

S7.1 Equivalent Circuit

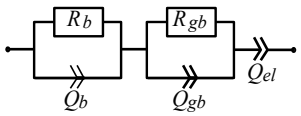

Figure S9: Bricklayer model for impedance data analysis Here, R_b and R_{gb} are the bulk and grain boundary resistance while Q_b, Q_{gb} and Q_{el} represent the constant phase element for the bulk, grain boundary and the electrode polarisation.[5]

S7.2 Ex-situ Impedance Measurements

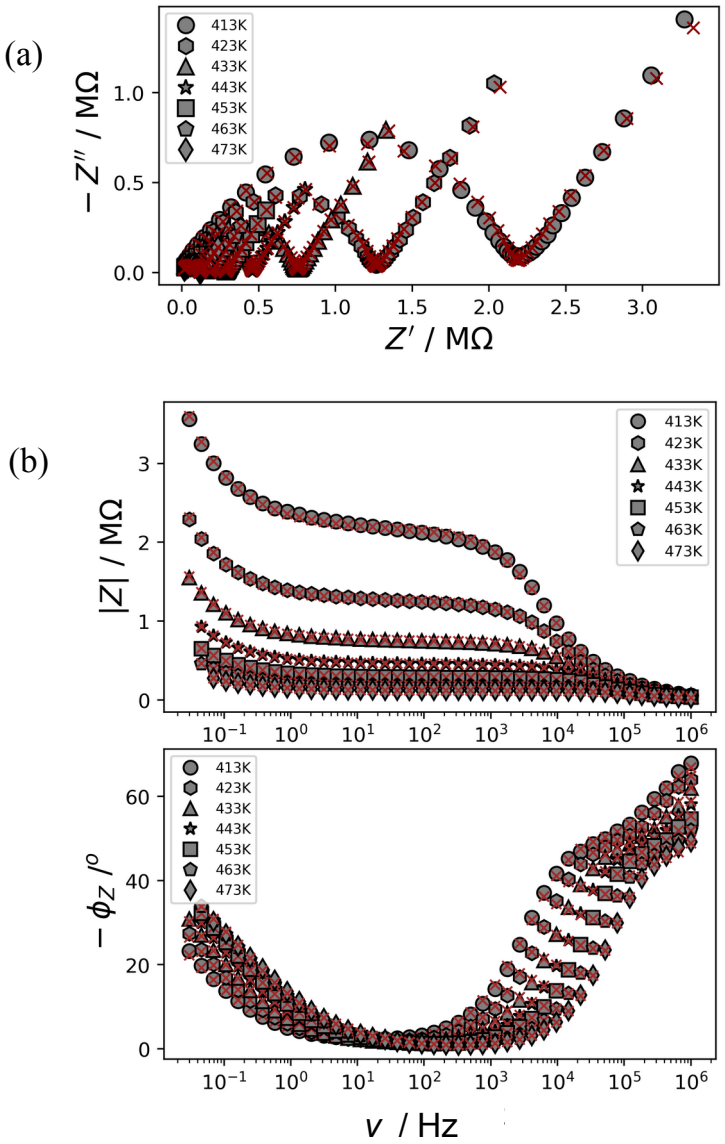

Figure S10: Nyquist (a) and Bode (b) plots of ex-situ impedance measurements of a Li_8SnO_6 pellet (diameter = 8 mm, thickness = 2.1 mm) in a temperature range from 413 K to 473 K, the red (x) markers represent the fitted values using the brick layer model as shown in Figure S9.

S7.3 In-situ Impedance Measurements

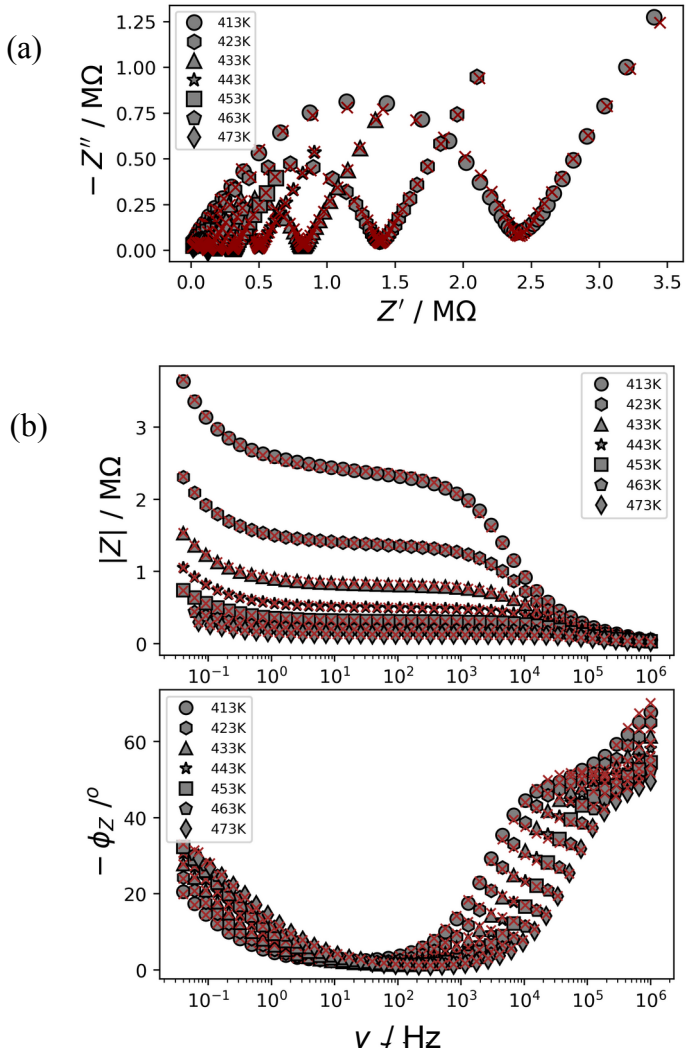

Figure S11: Nyquist (a) and Bode (b) plots of in-situ impedance measurement of Li_8SnO_6 pellet (diameter = 8 mm, thickness = 2.1 mm) at temperature range of 413 K – 473 K, the red (x) markers represent the fitted values using the brick layer model shown in Figure S9. Here, for the bulk region constant phase element Q_b is replaced with capacitance C_b.

S7.4 Ionic Conductivity

The ionic conductivity was estimated using the equation below;

$$\sigma = \frac{l}{RA} \qquad \text{S7.4.1}$$

Here, A is the cross-sectional area, and l is the thickness of the sample. The activation energy of the macroscopic ionic conductivity was obtained using below equation;

$$\sigma \cdot T = a_0 \exp\left(\frac{E_A}{k_B T}\right) \qquad \text{S7.4.2}$$

Here, a_0 is the pre-exponential factor, E_A the activation energy, k_B Boltzmann's constant, and T the temperature. The natural logarithmic of equation S7.4.2 was used to fit the experimental data (Figure S12)

$$\ln\left(\sigma \cdot T / (\mathrm{S \cdot K/cm})\right) = -\frac{E_A}{k_B \cdot T} + \ln\left(a_0 / (\mathrm{S \cdot K/cm})\right) \qquad \text{S7.4.3}$$

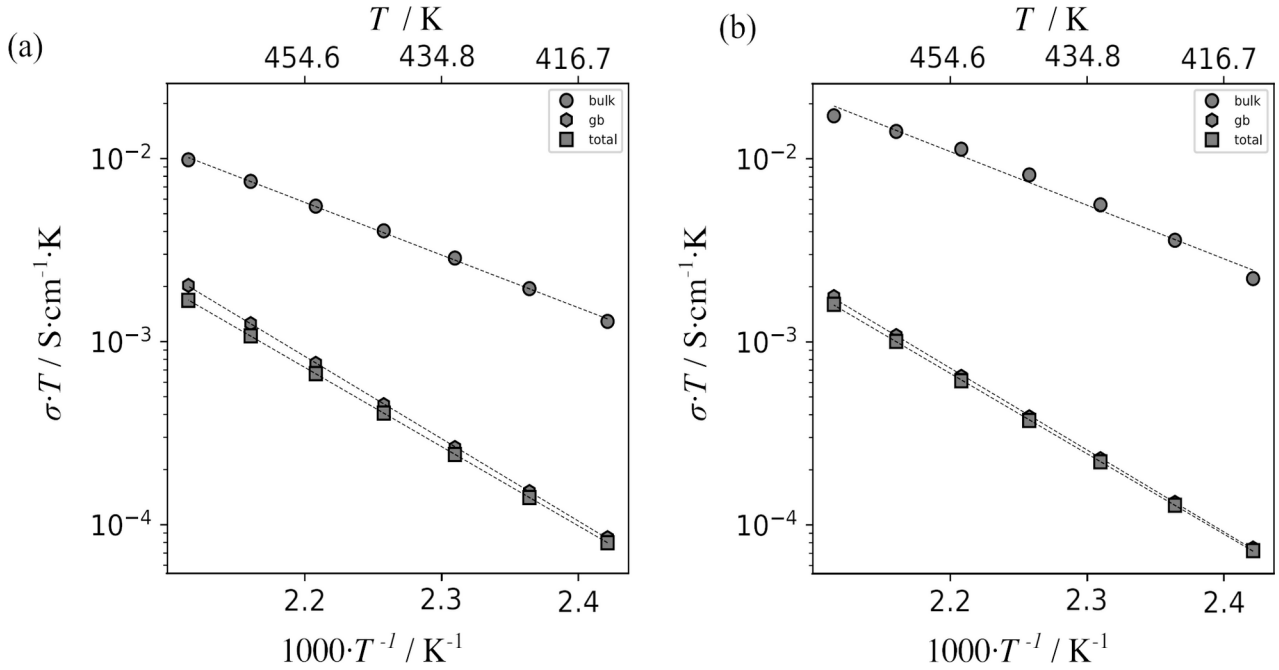

Figure S12: Product of the ionic conductivity σ and temperature T vs. inverse temperature plot for Li_8SnO_6 as measured using a standard, ex-situ impedance spectroscopy setup (a) and the described in-situ NMR-EIS setup (b). The results were obtained from impedance spectra in temperature range from 413 K to 473 K. Linear fits are indicated by dashed lines. The data points are indicated by grey circles, hexagons and squares which correspond to bulk, grain boundary and total ionic conductivity values, respectively. The obtained activation energies are shown in Table S3.

Table S3: Activation energies E_A from variable-temperature impedance spectroscopy (ex-situ & in-situ) measurement and analysis of Li_8SnO_6.

Impedance Spectroscopy Technique	**Conducting Region**	E_A**/eV**
Ex-situ	Bulk	0.569(8)
	Grain boundary	0.891(3)
	Total	0.857(1)
In-situ	Bulk	0.58(3)
	Grain boundary	0.885(6)
	Total	0.869(3)

Table S4: Comparison of in-situ NMR-EIS technique with ex-situ nuclear magnetic resonance and impedance spectroscopies conductivity studies of Li_8SnO_6. E_A is the activation energy from the in-situ NMR-EIS technique and ex-situ NMR and impedance spectroscopy experiments, respectively. While T_{onset} is the onset temperature from ^{7}Li NMR line shape analysis.

Techniques	**Assignment**	T_{onset}**/K**	**Ex-situ** E_A **/ eV**	T_{onset}**/K**	**In-situ** E_A **/ eV**
^{7}Li NMR Lineshape Analysis		385	0.62(4)	388	0.63(4)
^{7}Li NMR Spin-alignment Echo			0.61(1)		0.58(1)
Impedance Spectroscopy	Bulk		0.569(8)		0.58(3)
	Grain Boundary		0.891(3)		0.885(6)
	Total		0.857(1)		0.869(3)

S8 Nudged Elastic Band Calculations

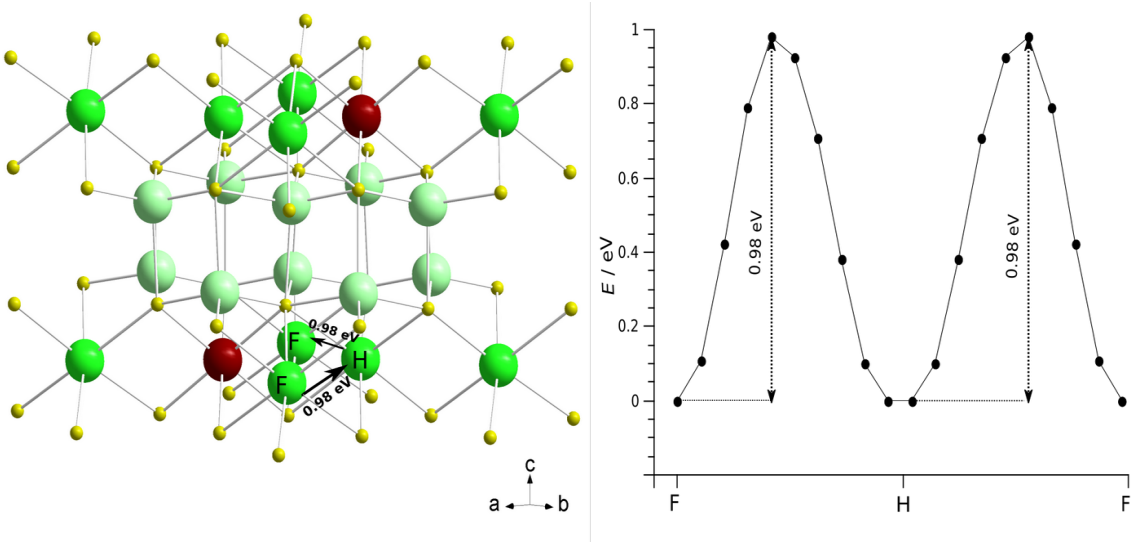

Figure S13: Potential pathways of vacancy-based Li vacancy migration and the associated activation energies determined by Nudged Elastic Band calculations. The Li vacancy diffusion through F→H→F and the corresponding migration energies for the local jumps through a complete unit cell of Li_8SnO_6 (left). The graph shows the energy barriers along the most favorable pathway and the points in the graph are different images along the path from one crystallographic orbit to the other for Li vacancy migration from F→H→F over the entire unit cell (right).

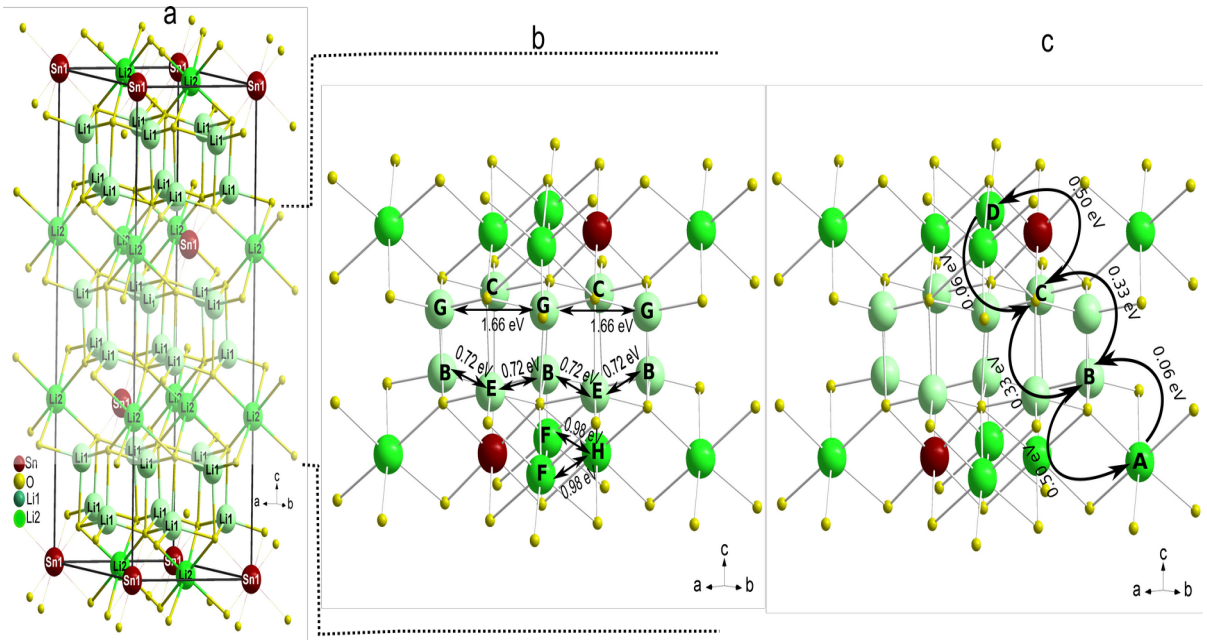

Figure S14: a) The crystal structure of Li_8SnO_6 with Li1, Li2, Sn and O sites. b) The figure shows the possible Li-diffusion transport routes from A→B→C→D , B→E, F→H→F and G→G through a complete unit cell of Li_8SnO_6. The solid arrows represent the possible Li ion diffusion pathways. Potential pathways of vacancy-based Li vacancy migration and the associated activation energies determined by Nudged Elastic Band calculations are also labeled in the figure.

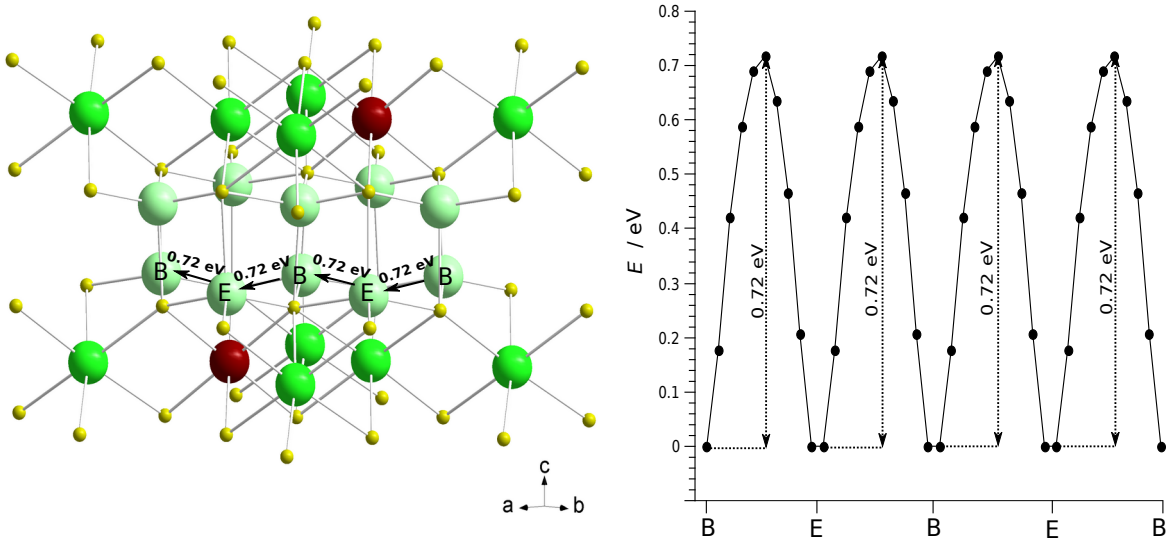

Figure S15: Potential pathways of vacancy-based Li vacancy migration and the associated activation energies determined by Nudged Elastic Band calculations. The Li vacancy diffusion through B→E→B→E→B and the corresponding migration energies for the local jumps through a complete unit cell of Li_8SnO_6 (left). The graph shows the energy barriers along the most favorable pathway and the points in the graph are different images along the path from one crystallographic orbit to the other for Li vacancy migration from B→E→B→E→B over the entire unit cell (right).

S9 Additional Simulation of NMR and EIS Channels decoupling

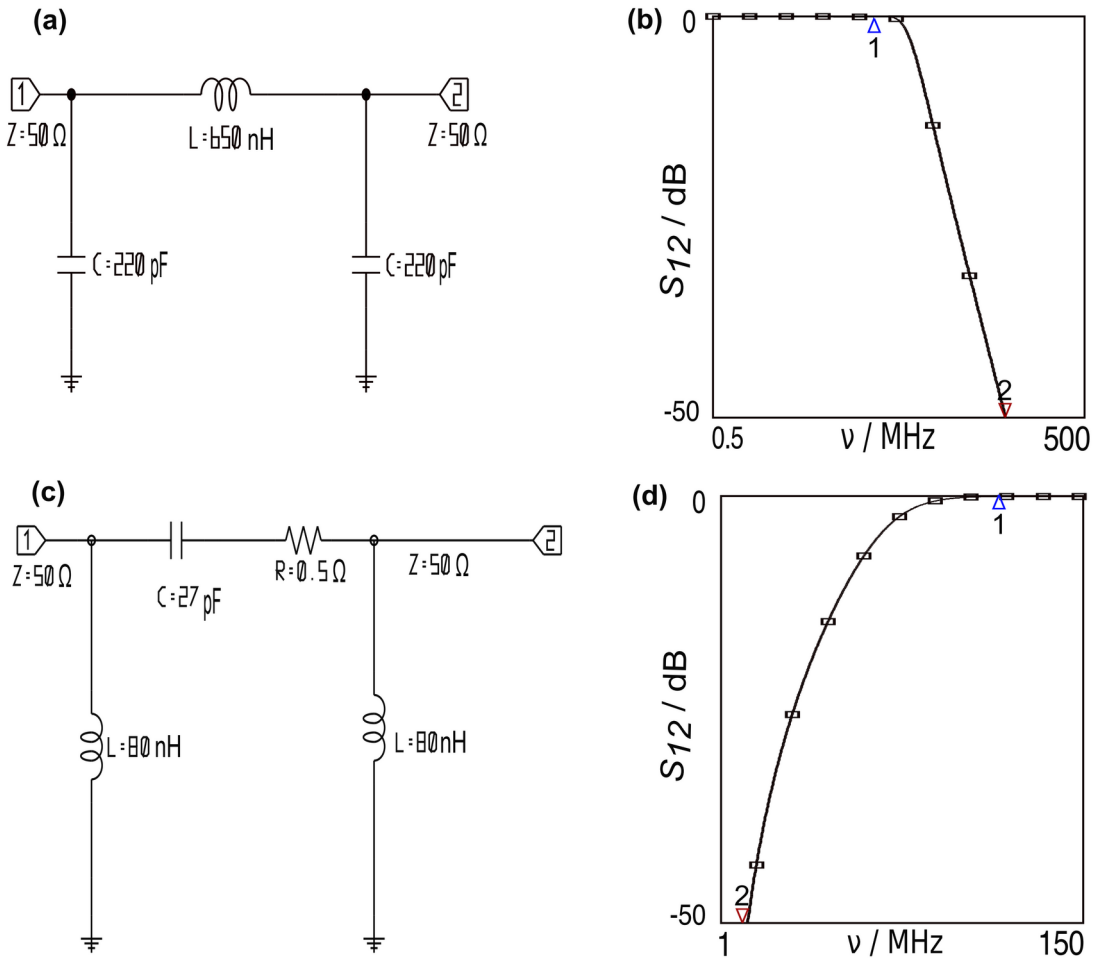

Figure S16: (a) LCR low pass filter circuit simulated to block NMR channel (116 MHz) (b) Simulated response of the low pass filter showing the attenuation of the NMR channel, achieved with at least 50 dB attenuation(red point 2) with a flat passband (<0.05 dB) at 10 MHz (blue point 1) (c) LCR high pass filter circuit simulated to block EIS channel (10 MHz) (d) Simulated response of the high pass filter showing the attenuation of the EIS channel with at least 50 dB (red point 2) and a flat passband (<0.05 dB) at 116 MHz (blue point 1). all simulations were performed using Vipec software v3.2.1.[3]

References

[1] M. Troemel, J. Hauck, *Z. Anorg. Allg. Chem.* **1969**, *368*, 248–253.

[2] M. Weiss, D. A. Weber, A. Senyshyn, J. Janek, W. G. Zeier, *ACS Appl. Mater. Interfaces* **2018**, *10*, 10935–10944.

[3] "ViPEC network analyser v3.1.2-1," can be found under https://sourceforge.net/projects/vipec/, **2013**.

[4] P. Virtanen, R. Gommers, T. E. Oliphant, M. Haberland, T. Reddy, D. Cournapeau, E. Burovski, P. Peterson, W. Weckesser, J. Bright, S. J. van der Walt, M. Brett, J. Wilson, K. J. Millman, N. Mayorov, A. R. J. Nelson, E. Jones, R. Kern, E. Larson, C. J. Carey, İ. Polat, Y. Feng, E. W. Moore, J. VanderPlas, D. Laxalde, J. Perktold, R. Cimrman, I. Henriksen, E. A. Quintero, C. R. Harris, A. M. Archibald, A. H. Ribeiro, F. Pedregosa, P. van Mulbregt, *Nat. Methods* **2020**, *17*, 261–272.

[5] J. T. S. Irvine, D. C. Sinclair, A. R. West, *Adv. Mater.* **1990**, *2*, 132–138.